Mechanical Systems and Signal Processing 239 (2025) 113326

Contents lists available at ScienceDirect

Mechanical Systems and Signal Processing

journal homepage: www.elsevier.com/locate/ymssp

Full Length Article

A large-stroke and adjustable-load magnetic quasi-zero stiffness isolator

Jun Yuan [a], Yunlai Zhou [a,*], Ying Zhang [b], Magd Abdel Wahab [c,d,*]

[a] State Key Laboratory for Strength and Vibration of Mechanical Structures, School of Aerospace Engineering, Xi'an Jiaotong University, Xi'an 710049, PR China
[b] State Key Laboratory for Manufacturing Systems Engineering, School of Instrument Science and Technology, Xi'an Jiaotong University, Xi'an 710049, PR China
[c] Soete Laboratory, Department of Electrical Energy, Metals, Mechanical Constructions, and Systems, Faculty of Engineering and Architecture, Ghent University, Belgium
[d] Parallel and Distributed Systems Laboratory, Jožef Stefan Institute, Jamova Cesta 39, SI-1000 Ljubljana, Slovenia

ARTICLE INFO

Keywords:
Quasi-zero stiffness
Large-stroke
Adjustable load
Magnetic constant-force
Low frequency isolation

ABSTRACT

Unlike traditional parallel structures that combine magnetic negative stiffness and positive stiffness, this study employs the principle of Lorentz force acting on a current-carrying coil in a uniform magnetic field to design a novel magnetic quasi-zero stiffness (QZS) isolator. The proposed isolator achieves both a wide QZS range and continuously adjustable load capacity by integrating the mechanisms of magnetic constant-force and magnetic repulsion-force, with the QZS characteristics primarily realized through the constant-force. The constant-force mechanism includes three magnets: two stator magnets generating a uniform magnetic field, and one moving magnet acting as a current-carrying coil. A constant Lorentz force is produced by placing one end of the moving magnet in the uniform magnetic field. The stroke and load capacity of the isolator depend on the field's spatial extent and intensity. The intensity can be adjusted by altering the overlap area of the stators. The magnetic repulsion boundary provides a hardening restoring force beyond the constant force region. Then, the effects of magnet parameters are discussed, and a dynamic model of the isolator incorporating equivalent viscous damping is established. Experimental results demonstrate that the proposed QZS isolator exhibits ultra-low resonant frequencies and large stroke, and verified the theoretical results.

1. Introduction

Vibration isolation has attracted considerable interest for its potential to improve equipment accuracy [1–3] and maintain structural safety [4,5]. Passive isolation has found widespread application due to its lack of external energy requirements and simple structure. To address the balance between stiffness and load capacity in linear isolators [6], nonlinear isolation theory [7] has advanced rapidly. Among the most extensively studied nonlinear isolation technologies is quasi-zero-stiffness (QZS) [8–10], which achieves near-zero dynamic stiffness through stiffness nonlinearity while maintaining the capacity to support static loads. This property, known as high-static-low-dynamic-stiffness (HSLDS), is central to QZS performance.

The most common QZS isolators integrate both positive and negative stiffness elements in parallel to attain nearly zero stiffness at

* Corresponding authors.
E-mail addresses: yunlai.zhou@xjtu.edu.cn (Y. Zhou), magd.abdelwahab@ugent.be (M. Abdel Wahab).

https://doi.org/10.1016/j.ymssp.2025.113326
Received 22 January 2025; Received in revised form 19 July 2025; Accepted 4 September 2025
Available online 11 September 2025
0888-3270/

the equilibrium position. In these designs, the negative-stiffness element plays a pivotal role. Typical implementations of negative stiffness include mechanical springs [8,11,12], buckling beams [13–15], negative stiffness magnetic springs [16–19], and cam-roller spring structures [20–22]. To improve the performance of isolators, substantial advancements have been made to negative stiffness structures. For instance, increasing the magnetic density of magnetic negative stiffness components can enhance the load capacity of QZS isolators. Wu et al. [23] proposed a magnet array with alternately arranged opposite polarities. Zhang et al. [24,25] introduced a high negative stiffness based on a Halbach magnet array, Wu et al. [26] presented a multi-tile magnetic spring with high negative stiffness, both achieving higher negative stiffness values than conventional magnetic configurations [16,17]. Zhao [27–29] proposed a QZS isolator utilizing multiple pairs of oblique springs, enabling the isolation of larger displacement excitations in comparison to a system with just one pair. Similarly, Ye et al. [30] introduced an optimized cam-roller-spring structure with multiple QZS regions for adapting to varying support loads. Yan et al. [31] presented a symmetric polygonal structure made up of two three-link assemblies, capable of sustaining linear negative stiffness across a broad displacement range and adjusting the load. Only adjusting the negative stiffness elements is insufficient for meeting the demands of various applications. Xie et al. [32] designed a QZS isolator that integrates pneumatic and electromagnetic mechanisms, controlling positive stiffness by adjusting air pressure and negative stiffness via current regulation.

Besides the parallel mechanisms of positive and negative stiffness, other mechanisms for achieving QZS have been proposed. Inspired by nature, beneficial nonlinearities found in biological structures have led to the development of bio-inspired isolators. Jing et al. [33–35] innovatively created a series of limb-like or X-shaped structures by mimicking biological limbs. Deng et al. [36], drawing inspiration from bird necks, developed a multi-layer QZS isolator that operates over a wide displacement range. Metamaterial-based QZS isolators have attracted considerable attention owing to their integrated structures, which effectively avoid the issues of Coulomb friction in assembly structures [37,38]. Liu et al. [39] discovered that truncated conical shell structures possess exceptional properties, such as excellent load-bearing ability and diverse mechanical responses. Through structural parameter optimization, they were able to generate nearly constant output forces and hardening boundary conditions over a wide displacement range, achieving ideal QZS characteristics. Lin et al. [40] designed a novel local resonance metamaterial by optimizing folded slender beams, which exhibit near-zero stiffness in three dimensions. Zhou et al. [41,42] developed a stackable multi-layer QZS structure by shaping folded slender beams. Zhang et al. [43], Zeng et al. [44] and Hou et al. [45] also achieved QZS by designing flexible curved beams, proposing multiple QZS modules in parallel or series to enable programmable working loads and operational ranges. Wu et al. [46] developed a mechanical metamaterial featuring quasi-zero stiffness, enabling vibration isolation across the entire frequency range, by using hexagonal hinges and mechanical springs. Sun et al. [47] ingeniously used a tensegrity structure to achieve torsional QZS isolator with a wide range. The integrated metamaterial structure is prone to fatigue damage in the long-term vibration environment.

Studies have shown that the stroke of QZS isolators is closely related to the width of the QZS region. Magnetic QZS isolators have been widely investigated due to their advantages of non-contact operation and low damping. The strong nonlinearity of the magnetic field leads to a relatively narrow QZS region, thus restricting isolator stroke. In most cases, the effective stroke of magnetic QZS isolators is confined to a narrow range of 1–2 mm [24,48–50]. Furthermore, since the properties of permanent magnets are fixed, the characteristics of magnetic QZS isolators are nearly non-adjustable. Therefore, expanding the QZS region, and improving adaptability to varying loads are critical challenges in enhancing the performance of magnetic QZS isolators.

Lu et al. [51] proposed load variation that can be achieved by altering the current in electromagnets. Qi et al. [52] introduced a system that integrates repulsive magnets to modulate positive stiffness with a sliding beam that provides negative stiffness, allowing for continuous adjustment of load capacity. Ji et al. [53] combined a magnetic negative stiffness structure with a displacement amplification system, successfully broadening the linear range of negative stiffness. Qi et al. [54] achieved constant force through the interaction between a magnetic rod and a high-permeability sleeve, and then combined with the stiffness-hardening boundary to achieve HSLDS characteristics. Liu et al. [55] proposed a magnetic higher-order QZS mechanism, which could produce a wider displacement range compared with the low-order QZS. These studies addressed only one of the two challenges, load adjustment or long stroke, while integrating both functionalities into a magnetic QZS isolator remains a challenge.

Our study proposes a novel magnetic QZS isolator that combines a magnetic constant-force structure with a magnetic repulsion boundary. Compared with the parallel combination of magnetic negative stiffness and positive stiffness, the proposed isolator offers both a larger stroke and adjustable load capacity. The concept of magnetic constant-force is inspired by the effect of a uniformly charged conductor experiencing a constant force in a uniform magnetic field. The proposed constant-force structure consists of three magnets: two serving as stators to generate a relatively uniform magnetic field, and a third magnet, which can be equivalently regarded as a charged coil placed within this field. The uniform magnetic field's range and intensity determine the working stroke and load capacity of the isolator. The field intensity, in particular, can be adjusted by modifying the overlapping area of the two stator magnets. Additionally, the introduction of the magnetic repulsion boundary serves to establish a hardening restoring force outside the constant-force region, facilitating the rapid return of the mover to its equilibrium position.

The organization of this article is as follows. Section 2 introduces the concept of the combined isolator and the principle of constant force generation. Section 3 derives the magnetic field and force models for the magnetic constant-force structure, and analyzes the impact of parameters as well as the principle of variable load. Section 4 presents the implementation of the nonlinear constraint boundary and the combined QZS isolator. To evaluate the performance of the proposed isolator, Section 5 conducts a numerical study of the transfer function using the harmonic balance method, considering the effects of Coulomb friction, viscous damping, and displacement excitation amplitude. Section 6 presents experimental validation of the proposed isolator. Finally, Section 7 offers conclusions and discussions.

2. Conceptual design and principle

This section presents the conceptual design of the combined magnetic QZS isolator and the principle of magnetic constant-force generation. Fig. 1 shows that the isolator primarily comprises two key components: a magnetic constant-force (MCF) structure and a magnetic repulsion-force (MRF) structure. The MCF structure provides quasi-zero stiffness and load-bearing capacity, while the MRF structure generates a hardening nonlinear restoring force. The force–displacement curve generated by the combination of these two structures exhibits the characteristics of high static and low dynamic stiffness (HSLDS).

Within the combined isolator, the magnetic constant-force structure is critical. It consists of three elongated magnets arranged in parallel. According to Ampère's law, a charged conductor in a uniform magnetic field experiences a constant force, as illustrated in Fig. 1(a). This principle is similarly applicable to the magnetic constant-force structure. Magnetic field modeling methods for magnets include the equivalent charge model [56,57] and the equivalent current model [17]. To intuitively explain the constant force principle, the two stator magnets are modeled using the equivalent charge model, while the mover magnet is equivalent to a coil with a current density J. Fig. 1(b) presents the schematic of the equivalent modeling for the stator and mover magnets. It is evident that a uniform magnetic field directed horizontally to the right is generated in the central region between the two stator magnets. The mover magnet can be equivalently represented as the equivalent coil in Fig. 1(b), based on its magnetization direction. The bottom end of the equivalent coil is located in the stators' uniform magnetic field. According to Ampère's law, this end generates a constant upward force F_{z1}. In contrast, the top end of the equivalent coil is far from the magnetic field, where the field strength is relatively weak, resulting in an almost negligible force F_{z3}. The front and rear ends of the equivalent coil experience forces of equal magnitude but opposite directions, in and out of the plane, respectively. Therefore, the total magnetic force acting on the mover magnet can be approximated as a

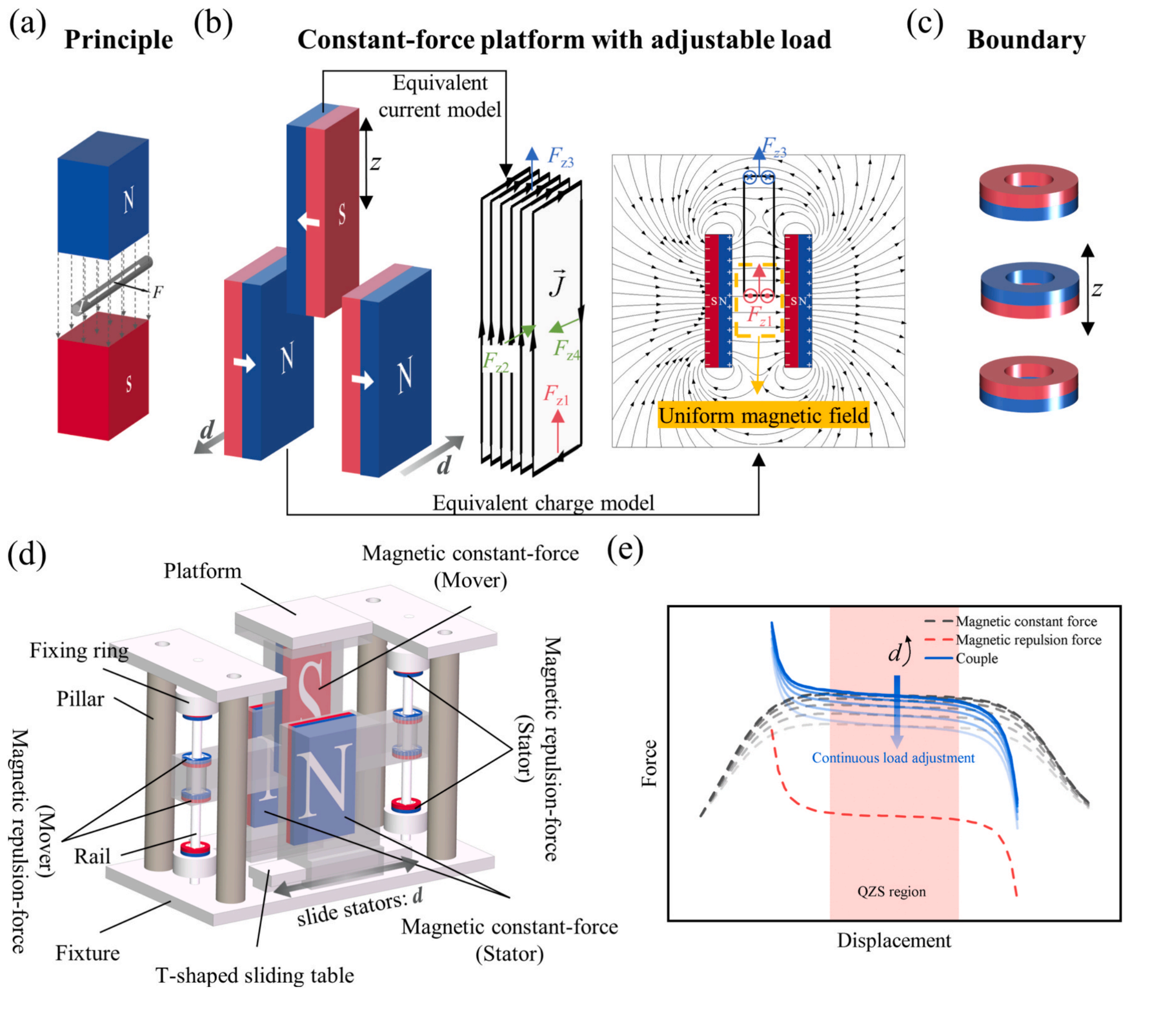

Fig. 1. Principle and structural schematic diagram of magnetic-constant force isolator: (a) Principle of magnetic constant force, (b) three-magnet configuration for realizing magnetic-constant force and schematic diagram of equivalent model, (c) nonlinear hardening boundary, (d) 3D structural diagram of vibration isolator and (e) force-displacement relation between local and global structures.

constant force. The detailed calculation of magnetic field strength and magnetic force will be presented in Section 3.

3. Modeling and analysis of the constant force magnet array

3.1. Basic parameters of the magnet array structure

The basic parameters of the magnetic constant-force array are illustrated in Fig. 2, and the initial values are listed in Table 1. The magnets are made of NdFeB, N35.

3.2. Magnetic field distribution of the stators

The key to achieving magnetic constant-force lies in the creation of a uniform magnetic field. To intuitively demonstrate the process of generating this uniform magnetic field, the equivalent charge model is utilized. This model introduces a hypothetical magnetic charge, analogous to an electric charge, with magnetic flux lines extending from positive to negative magnetic charges. The magnetic flux at any point in space can be determined using the magnetic Coulomb's law. Fig. 3(a) depicts a permanent magnet with a magnetization intensity M, where the magnetization direction is horizontally oriented to the right.

Assuming uniform magnetization and applying the equivalent charge theory [56,57], the volumetric magnetic charge density ρ_m within the magnet is zero, while only the surface magnetic charge density σ_m exists on the plane perpendicular to the magnetization vector. Under the assumption of relative permeability $\mu_r = 1$, the surface magnetic charge density σ_m is expressed as:

$$\sigma_m = \vec{M} \cdot \vec{n} = \frac{B_r}{\mu_0} \tag{1}$$

where $\vec{M}$ represents the remanent magnetization intensity, $\vec{n}$ is the unit vector normal to the surface of the magnet, B_r is the remanent magnetic flux density, and μ_0 is the vacuum permeability, with a constant value of $4\pi \times 10^{-7}$ Wb/(A•m).

In Fig. 3(a), the magnetic charge surfaces of the rectangular permanent magnet correspond to the two planes perpendicular to the magnetization direction. According to magnetic Coulomb's law, the magnetic flux density vector $\vec{B}$ at the observation point Q, generated by the magnetic charge at the source point P, is given by:

$$\mathrm{d}\boldsymbol{B}(\vec{r}) = \frac{\mu_0}{4\pi} \frac{\sigma_m \cdot \vec{r}}{|\vec{r}|^3} \mathrm{d}y\mathrm{d}z \tag{2}$$

where $\vec{r}$ denotes the vector pointing from P to Q, i.e. $|\vec{r}| = \sqrt{(x_1 - x_0)^2 + (y_1 - y_0)^2 + (z_1 - z_0)^2}$.

The overall magnetic flux density at the observation point Q, produced by the entire magnet, can be calculated by integrating Eq. (2):

$$\boldsymbol{B}(\vec{r}) = \int_0^l \int_0^h \frac{\mu_0}{4\pi} \frac{\sigma_m \cdot \vec{r}}{|\vec{r}|^3} \mathrm{d}y\mathrm{d}z - \int_0^l \int_0^h \frac{\mu_0}{4\pi} \frac{\sigma_m \cdot \vec{r}'}{|\vec{r}'|^3} \mathrm{d}y_0\mathrm{d}z_0 \tag{3}$$

where $\vec{r}$ and $\vec{r}'$ denote the displacements from the corresponding points on the positive and negative magnetic charge regions to the observation point, respectively.

For the structure shown in Fig. 1 (b), to calculate the magnetic force in the z-component on the mover magnet, the magnetic flux density generated by the stator magnets in the x-component needs to be computed. Eq. (2) is modified as follows:

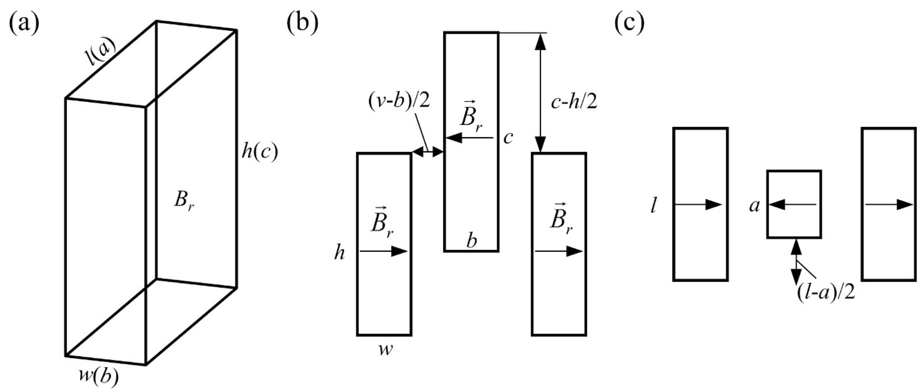

Fig. 2. Magnet array parameter labels: (a) Magnet dimension parameters, (b) front view (equilibrium position) and (c) top view.

Table 1
Basic parameters of the magnetic constant-force array.

Parameter Name	Symbol	Value unit	Unit
Remanent magnetic flux density	B_r	1.15	T
Stator length	l	30	mm
Stator width	w	5	
Stator height	h	50	
Mover length	a	20	
Mover width	b	10	
Mover height	c	60	
Stator gap	v	22	

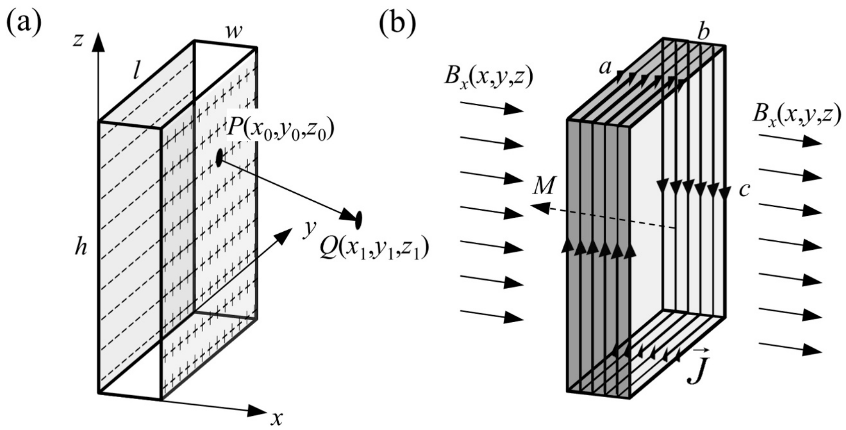

Fig. 3. Schematic diagram of (a) the equivalent charge model and (b) the equivalent current model.

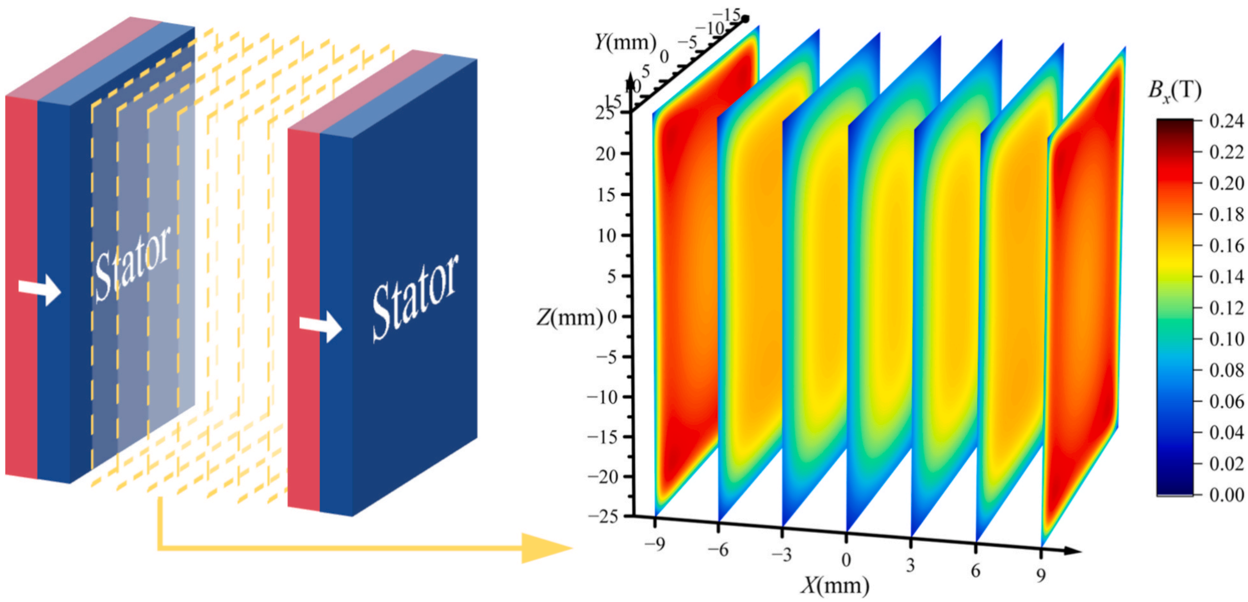

Fig. 4. Magnetic flux density distribution of the x-component between the stator magnets.

$$\mathrm{d}B_x(x_1, y_1, z_1) = \frac{\mu_0}{4\pi} \frac{\sigma_m \cdot (x_1 - x_0)}{\left(\sqrt{(x_1 - x_0)^2 + (y_1 - y_0)^2 + (z_1 - z_0)^2}\right)^3} \mathrm{d}y_0 \mathrm{d}z_0 \tag{4}$$

The magnetic field produced by the stator is calculated through numerical methods. Fig. 4 illustrates the magnetic flux density distribution at different cross-sections between the two stator magnets. It is clear that the field remains mostly uniform in the central area between them.

3.3. Magnetic force calculation on the mover magnet

Fig. 3(b) shows the equivalent coil model of the mover magnet. According to the equivalent current theory [17], the magnet can be simplified to a volume current density J_m and a surface current density J_s. Under the assumptions of relative permeability $\mu_r = 1$ and uniform magnetization, the volume current density J_m is equal to 0, while surface current density is given by:

$$\boldsymbol{J} = \vec{M} \times \vec{n} = \frac{\vec{B}_r}{\mu_0} \times \vec{n} \tag{5}$$

where a current element is taken, the Ampère force acting on it in the magnetic field is expressed as:

$$\mathrm{d}\boldsymbol{F}(\vec{r}) = \boldsymbol{J}\mathrm{d}s \times \boldsymbol{B} \tag{6}$$

For the model in Fig. 1 (b), it is evident that only the top and bottom ends of the equivalent coil experience the z-component of the Ampère force. The total magnetic force in the z-direction is given by:

$$F_z = \int_0^a \int_0^b J_y \times B_{x,Lower}(x, y, z)\mathrm{d}x\mathrm{d}y - \int_0^a \int_0^b J_y \times B_{x,Upper}(x, y, z)\mathrm{d}x\mathrm{d}y \tag{7}$$

Substituting Eq. (1)–(6) into Eq. (7) gives:

$$F_z = \frac{B_r^2}{4\pi\mu_0} \sum_{i=0}^{1} \sum_{j=0}^{1} \sum_{k=0}^{1} \sum_{p=0}^{1} \sum_{q=0}^{1} \sum_{r=0}^{1} (-1)^{i+j+k+p+q+r} \phi(U, V, W, R) \tag{8}$$

where

$$\begin{gathered} i, j, k, p, q, r \in \{0, 1\} \\ U = x_c + (-1)^i w/2 - (-1)^p b/2 \\ V = y_c + (-1)^j l/2 - (-1)^q a/2 \\ W = z_c + (-1)^k h/2 - (-1)^r c/2 \\ R = \sqrt{U^2 + V^2 + W^2} \\ \phi(U, V, W, R) = \frac{1}{2}(V^2 - U^2)\ln(R + W) + VW\ln(R + V) - UV\arctan\left(\frac{VW}{RU}\right) - \frac{1}{2}RW \end{gathered} \tag{9}$$

x_c, y_c, z_c represent the distance between the centers of two magnets.

In Fig. 5, the calculated results of the magnetic forces at the bottom (F_{z1}) and top (F_{z3}) correspond to $r = 0$ and $r = 1$ in Eq. (8),

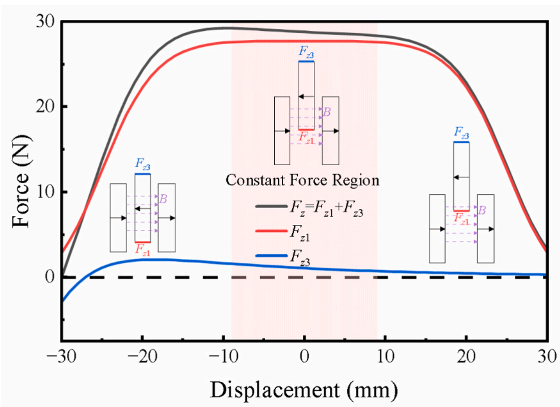

Fig. 5. Forces on the bottom and top ends of the equivalent coil.

respectively. When the bottom equivalent current surface of the mover is located within the uniform magnetic field region of the stators, it experiences a constant upward force. In contrast, the top equivalent current surface is far from the magnetic field, resulting in a negligible force. The constant-force region approximately covers ± 9 mm. Strictly speaking, the MCF region exhibits slight nonlinearity rather than absolute zero stiffness. When combined with boundary structures, this minor nonlinearity remains well within acceptable limits for isolator applications.

3.4. Influence of structural parameters on mechanical performance

This section investigates the influence of structural parameters on the force–displacement curve. To evaluate the impact of each parameter, the mover's structural parameters are fixed while the stator parameters are varied. Due to the strong nonlinearity of magnetic force, the approximate constant-force region is rigorously defined as:

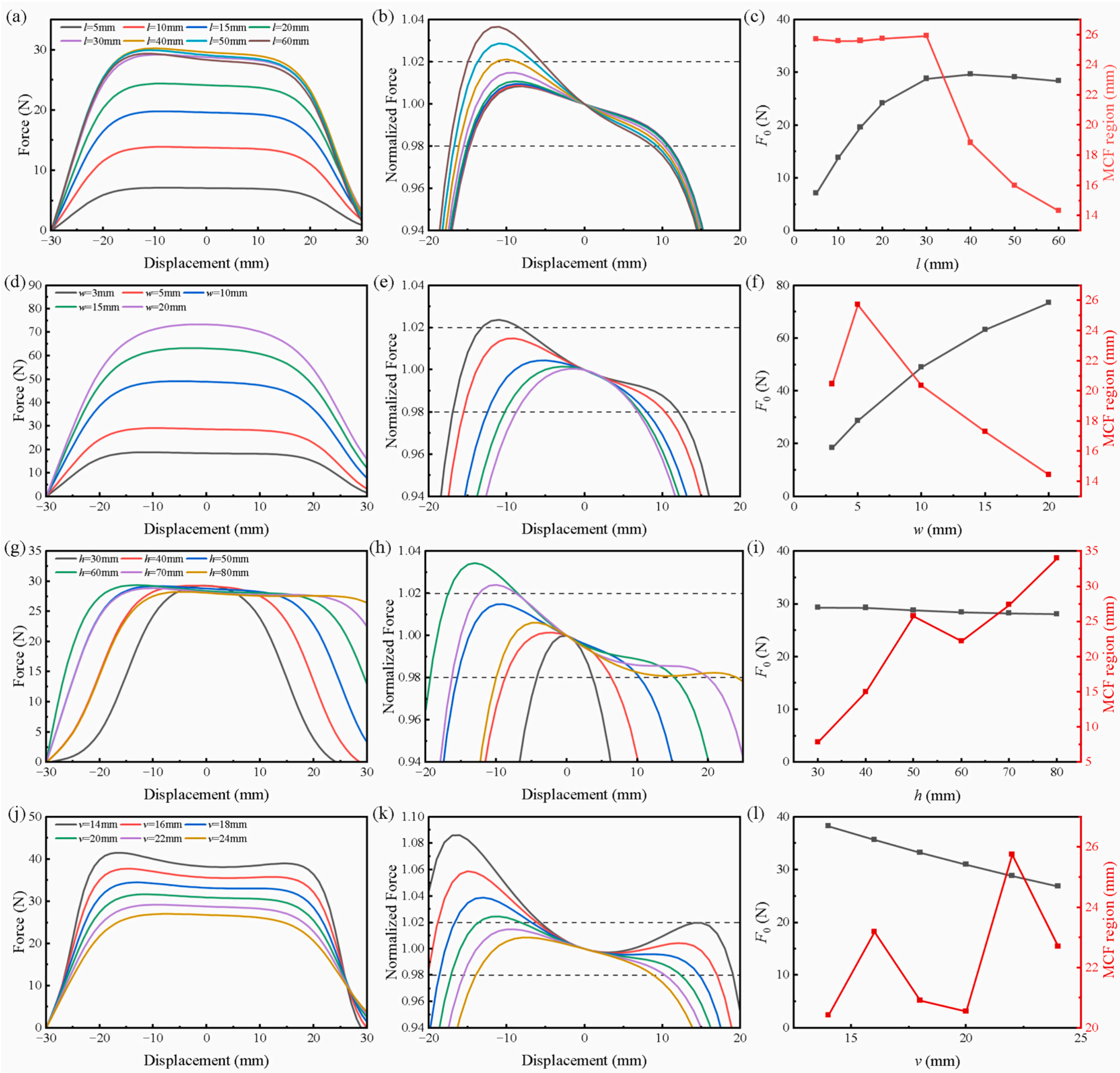

Fig. 6. The influence of magnet parameters on magnetic force and stiffness: (a)(d)(g)(j) Magnetic force curve, (b)(e)(h)(k) normalized Magnetic force curve and (c)(f)(i)(l) load F_0 and MCF region.

$$Z = \left\{ z \left| \left| \frac{F(z) - F_0}{F_0} \right| \leqslant \varepsilon \right. \right\}$$
$$\delta = \max(Z) - \min(Z) \tag{10}$$

where, F_0 is the load at equilibrium position ($z = 0$, as shown in Fig. 2(b)), $F(z)$ is the force at displacement z and ε is an acceptable threshold. Here, ε is set to 0.02.

Fig. 6(a) presents the magnetic force curves for different stator's length (l), with l ranging from 5 to 60 mm. When $l \leq 30$ mm, increasing the stators' length enhances the load capacity at the equilibrium position while maintaining a nearly constant width of the MCF region. However, for $l > 30$ mm, the MCF magnitude slightly decreases with a rapidly narrowing MCF region. Although the force curves for $l = 30$–60 mm appear similar in Fig. 6(a), this similarity diminishes after normalization, as shown in Fig. 6(b). The enhanced contrast in the normalized curves reveals growing force-profile nonlinearity with increasing l, along with significant stiffness variations.

The effects of other stator parameters, width (w), height (h), and air gap (v), are also investigated. Fig. 6(d)–(f) show that increasing w from 5 to 20 mm substantially elevates F_0. The width of the MCF region expands when $w \leq 5$ mm, but contracts when $w > 5$ mm.

As shown in Fig. 6(g)–(i), the load slightly decreases with increasing stator height h, while the width of the MCF region follows a three-phase pattern: initial increases, subsequent decreases, and final increases again. The intermediate reduction primarily results from enhanced force-profile nonlinearity and threshold ε effects. Detailed examination of Fig. 6(h) reveals that this process is also accompanied by a spatial shifting of the MCF region, initially expanding around $z = 0$, then shifting rightward. This behavior correlates with the h/c ratio, where larger h extends the uniform magnetic field at the mover's lower end. When $h > c$, the mover's upper end requires greater upward displacement to exit the field, causing the observed rightward shift.

Fig. 6(j)–(l) illustrate air gap v effects, showing high sensitivity to both load magnitude and stiffness nonlinearity. Increasing v consistently reduces load, while the MCF region width shows no monotonic trend due to pronounced nonlinearity at small v values that excludes most force curves from the threshold range. A clear decreasing trend in MCF width emerges only when $v \geq 22$ mm.

These findings emphasize the influence of key magnet design parameters on magnetic force and stiffness. The MCF region is a crucial factor in the subsequent construction of the QZS region of the isolator. The magnitude of the constant force determines the load-bearing capacity of the isolator, the extent of the force region defines its operating stroke, and the nonlinear stiffness within the MCF region directly affects the nonlinear response characteristics of the isolator.

3.5. Adjustment of load

Based on Eq. (5), and assuming an ideally uniform magnetic field, both B_x and J_y can be considered as constants. Neglecting the force at the top end of the equivalent coil, Eq. (7) is modified as follows:

$$F_z = J_y B_x \int_0^a \int_0^b \mathrm{d}x\mathrm{d}y = J_y B_x S \tag{11}$$

where S denotes the area at the bottom end of the mover that is within the uniform magnetic field.

Thus, the load can be adjusted by changing the strength of the uniform magnetic field. This can be achieved by sliding the stator. Fig. 7(a) depicts the magnetic force curves and corresponding loads ($F_{z=0}$) for different sliding distances of the stators. As the sliding distance increases, the magnetic constant-force decreases slowly at first, and then drops rapidly when $d > 4$ mm. The relation between the load and sliding distance d follows a quadratic function. Notably, this method of variable load does not change the range of the constant force.

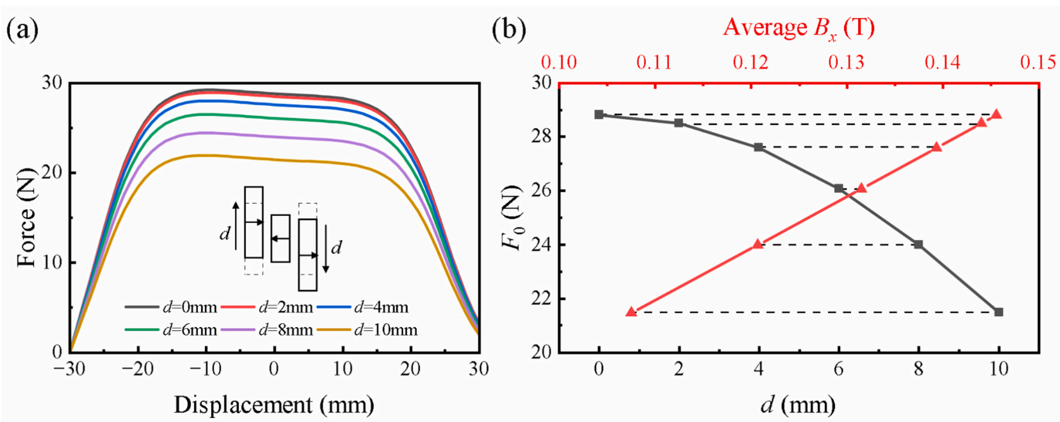

Fig. 7. (a) Force-displacement curves for different sliding distances and (b) relation of the load with sliding distance d and average magnetic flux density Bx, respectively.

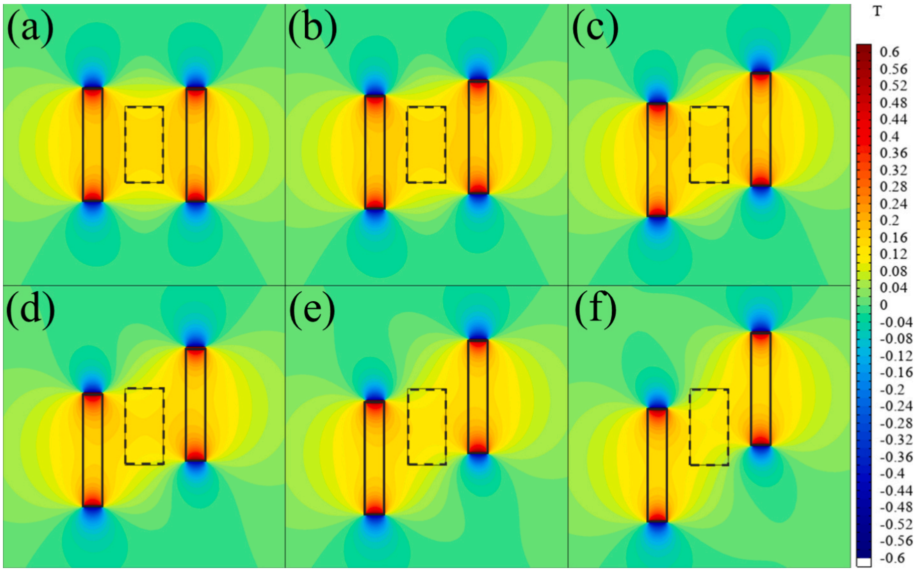

Fig. 8. Contour plots of the x-component magnetic flux density generated by the stator magnets at different translation distances: (a) $d = 0$ mm, (b) $d = 2$ mm, (c) $d = 4$ mm, (d) $d = 6$ mm, (e) $d = 8$ mm and (f) $d = 10$ mm.

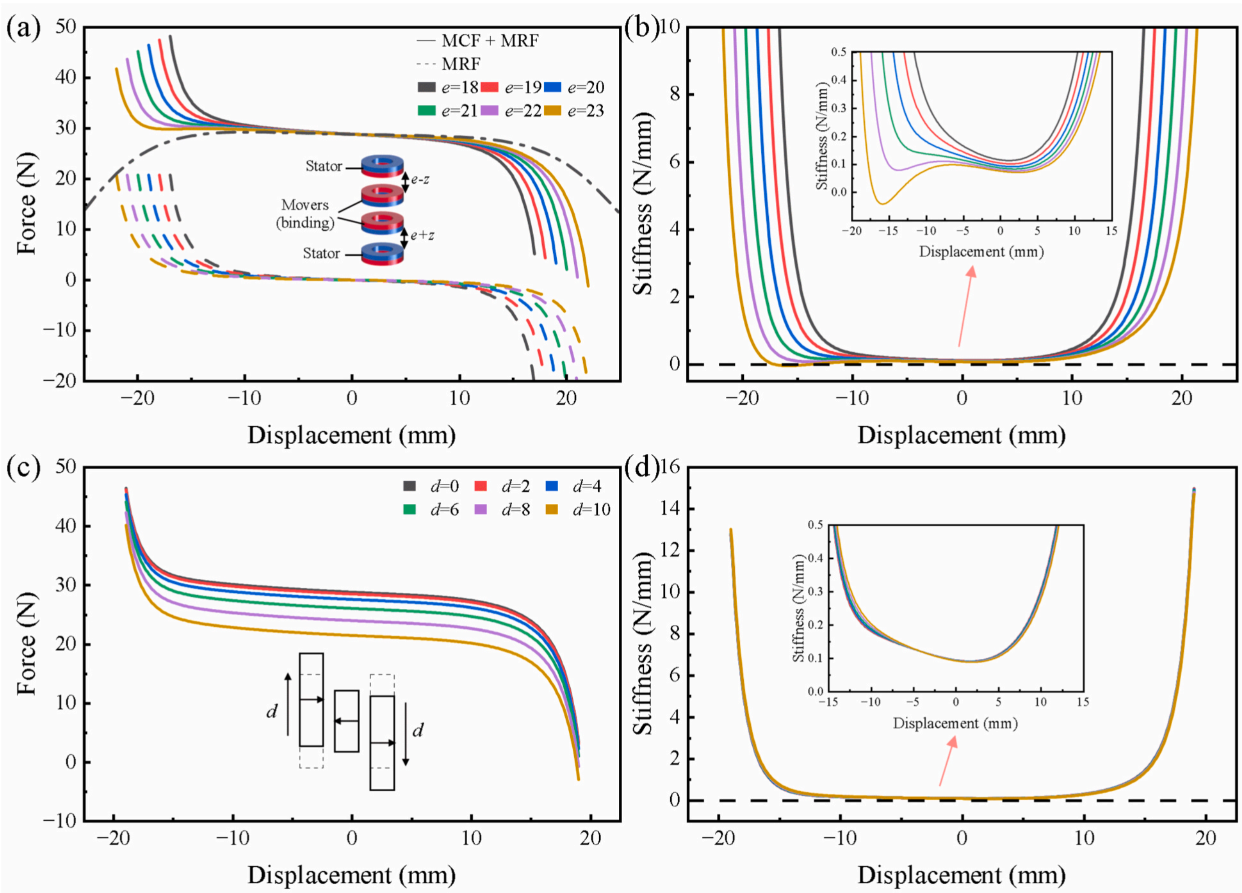

Fig. 9. (a), (b) Force and stiffness curves for the combination of the magnetic repulsion boundary and the magnetic constant-force ($d = 0$ mm) and (c), (d) force and stiffness curves for the combination of different loads and the magnetic repulsion boundary ($e = 20$ mm).

The load is strongly dependent on the magnetic flux density within the space occupied by the mover. Fig. 8 illustrates the variation of the x-component of the magnetic flux density (B_x) within the projection space of the mover for different sliding distances of the stators. When the sliding distance d is small, the flux density B_x in the mover's region changes minimally, and most of the space is still in the uniform magnetic field, which is attributable to the stators being longer than the mover. As the sliding distance d increases, the overlapping area between the two stators diminishes, leading to a rapid reduction in B_x, and the load F begins to decrease. Fig. 7(b) further demonstrates the relation between the load and the average magnetic flux density in the mover's region, revealing a linear correlation, which is consistent with the conclusion in Eq. (11).

4. Investigation of force and stiffness characteristics of the composite structure

4.1. Nonlinear constraint boundaries and implementation of the combined QZS

Section 3 detailed the force–displacement curve of the MCF structure, demonstrating its capability for low-frequency vibration isolation within the constant force range. Beyond this range, the force–displacement relation fails to offer adequate restoring force for the mover. Qi et al. [54] introduced repulsive cylindrical magnets as a hardening boundary condition for vibration isolators, which proved effective.

To enhance structural compactness, this study uses four pairs of repulsive ring-shaped magnets as boundary conditions, with two pair serving as the upper boundary and the other two as the lower boundary. The two ring magnets in the middle, acting as the movers, are bound together, as illustrated in Fig. 9(a). Due to the repulsive nature of the magnets, the force increases as the gap decreases, thereby providing a progressively hardening constraint boundary as the mover shifts upward or downward. The ring magnets are made of NdFeB (N35) with dimensions of D12 × D6 × 3 mm.

Fig. 9(a) demonstrates the force–displacement curves for varying magnetic ring gap distances e, as well as the resulting magnetic force curves obtained by superimposing the MRF of these gap distances with the MCF ($d = 0$ mm). Fig. 9(b) further presents the stiffness-displacement curves.

When the gap e is small, the stiffness at the equilibrium position of the composite structure increases. In contrast, larger gaps result in reduced stiffness but greater asymmetry in the stiffness profile. This asymmetry not only complicates the polynomial fitting of the magnetic force curve but also introduces more complex nonlinear behavior into the vibration isolator. Furthermore, negative stiffness may occur, as observed for $e = 23$ mm in Fig. 9(b), which can lead to instability. Therefore, for subsequent experimental verification, an optimal gap of $e = 20$ mm is selected, as its stiffness-displacement curve exhibits a relatively flat bottom.

Fig. 9(c) and (d) present the force and corresponding stiffness curves obtained by combining different stators' sliding distances d with a fixed magnetic ring gap of $e = 20$ mm. It can be observed that under varying load conditions, the magnetic constant-force remains well-aligned with the magnetic repulsion boundary, while the stiffness characteristics remain nearly unchanged. In terms of stiffness values, when $d = 0$ mm and $e = 20$ mm, the stiffness k_0 of the composite structure at the equilibrium position is extremely low, i.e. 0.095 N/mm. This aligns with the concept of "quasi-zero stiffness".

4.2. Comparison with benchmark studies

In this section, the proposed magnetic QZS is compared with three different types of magnetic QZS configurations: (a) QZS achieved through magnetic constant-force, (b) QZS formed by the combination of magnetic repulsion and attraction, and (c) QZS realized through parallel-connected magnetic negative stiffness and linear positive stiffness elements.

To evaluate the performance of magnetic QZS, three key factors should be considered: the width of the QZS region, the size effect of the isolator, and the load density (the load provided only by the magnetic components). Based on these considerations, the following evaluation criteria are proposed.

(i) QZS region δ.

QZS means that the stiffness is close to zero. The smaller the stiffness, the smaller the force variation is. Therefore, the QZS range is defined as:

$$Z = \left\{ z \left| \left| \frac{F(z) - F_0}{F_0} \right| \leqslant \varepsilon \right. \right\} or Z = \{ z || F(z) | \leqslant \varepsilon mg \}, \varepsilon = 0.05$$
$$\delta = \max(Z) - \min(Z) \tag{12}$$

where F_0 is the load at equilibrium position, $F(z)$ is the force at displacement z, ε is an acceptable threshold and $\delta_{0.05}$ represents the QZS range when ε is set to 0.05.

(ii) QZS relative region η.

The QZS region primarily depends on the vibration isolator's dimension along the vibration direction. Since the spatial scales vary significantly across reference studies, a dimensionless parameter is introduced to evaluate the QZS range.

$$\eta = \frac{\delta}{L} \tag{13}$$

where L represents the maximum allowable range of motion for the mover.

(iii) Load density ρ.

A key characteristic of magnetic vibration isolators is the efficiency of magnetic array utilization. For instance, in the field of magnetic negative stiffness, researchers have consistently focused on achieving higher negative stiffness with smaller magnet volumes. Correspondingly, if the QZS load is directly supplied by the magnetic array, it is essential to evaluate the load utilization efficiency:

$$\rho = \frac{F_0}{VB_r^2} \tag{14}$$

where V denotes the volume of the magnetic array, B_r denotes the remanent magnetic flux density.

The comparison results are shown in Table 2. The results indicate that the magnetic constant-force type QZS vibration isolator (reference [54] and the proposed design) shows wider relative QZS range compared to those reported in references [55] and [24]. While compared to reference [54], the relative range of the proposed QZS is slightly higher, but its load density is 1.9 times higher. Since the isolators reported in references [55] and [24] do not utilize magnetic components to provide the load-bearing capacity, a comparison of load density is not applicable.

5. Theoretical analysis of vibration isolation performance

5.1. Dynamic modeling

To evaluate the performance of the proposed isolator, a dynamic model of the combined QZS isolator is established. Fig. 10 illustrates the schematic of the proposed isolator model. The dynamic response of the isolator in the vertical direction is represented by the following equation:

$$m\ddot{y} + c\dot{y} + fsgn(\dot{y}) + k_1 y + k_3 y^3 + k_5 y^5 + k_7 y^7 + k_9 y^9 = -m\ddot{y}_0 \tag{15}$$

where m represents the load mass, c denotes the viscous damping coefficient, and f is the Coulomb friction force. The stiffness coefficients k_1–k_9 correspond to the polynomial fittings of the magnetic force curve. y_0 is the displacement excitation applied to the isolator's base, and y_1 is the absolute displacement response generated by the mass m. The relative displacement $y(t)$ is given by $y(t) = y_1(t) - y_0(t)$.

Assuming the oscillator undergoes harmonic motion and the Coulomb friction force is constant, it can be replaced by an equivalent viscous damping. By equating the work done by all damping forces over one cycle to the work done by an equivalent viscous damping force, the following equation can be derived:

$$\int_0^T c_e\dot{y}\dot{y}\mathrm{d}t = \int_0^T (fsgn(\dot{y}) + c\dot{y})\dot{y}\mathrm{d}t \tag{16}$$

where T and Y represent the period and amplitude of the harmonic motion, and c_e denotes the equivalent viscous damping. The displacement is given by $y(t) = Y\cos(\omega t)$. Therefore, c_e is expressed as:

$$c_e = \frac{4f}{\pi Y\omega} + c \tag{17}$$

The amplitude-frequency response of the isolator can be approximated by deriving the first-order analytical solution through the harmonic balance method. By substituting $y(t) = Y\cos(\omega t)$, $y_0(t) = A\cos(\omega t + \theta)$ into Eq. (15) and applying the trigonometric function reduction formula:

Table 2
Parameters of the proposed QZS and the benchmark studies.

Type	Reference 1 [54] **(Magnetic constant-force)**	Reference 2 [55] **(Magnetic repulsion and attraction)**	Reference 3 [24] **(Magnetic negative stiffness)**	**The proposed design (Magnetic constant-force)**
Load (N)	15.3	13.35	29.4	28.8
Stiff ness k_0 (N/m)	46.81	36	120	95
Motion range of the mover L (mm)	80	180	10	40
QZS region $\delta_{0.05}$ (mm)	36.6	30.4	2.1	20.8
QZS relative region $\eta_{0.05}$	0.46	0.17	0.21	0.52
Remanence B_r (T)	1.21	The load is not supplied by the magnetic components.		1.15
Volume of magnetic components (mm^3)	17,769			19,500
Load density ρ ($N/mm^3/T^2$)	5.88×10^{-4}			1.11×10^{-3}

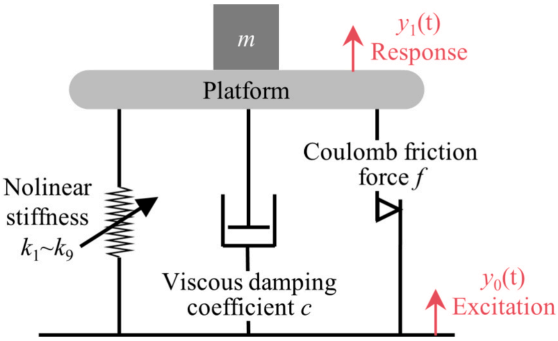

Fig. 10. Simplified model of the QZS isolator.

$$\begin{cases} \cos^3\omega t = \frac{3}{4}\cos\omega t + \frac{1}{4}\cos 3\omega t \\ \cos^5\omega t = \frac{10}{16}\cos\omega t + \frac{5}{16}\cos 3\omega t + \frac{1}{16}\cos 5\omega t \\ \cos^7\omega t = \frac{35}{64}\cos\omega t + \frac{21}{64}\cos 3\omega t + \frac{7}{64}\cos 5\omega t + \frac{1}{64}\cos 7\omega t \\ \cos^9\omega t = \frac{126}{256}\cos\omega t + \frac{84}{256}\cos 3\omega t + \frac{36}{256}\cos 5\omega t + \frac{9}{256}\cos 7\omega t + \frac{1}{256}\cos 9\omega t \end{cases} \tag{18}$$

Neglecting higher-order terms, the coefficients of the first-order harmonic terms $\sin(\omega t)$ and $\cos(\omega t)$ are as follows:

$$-m\omega^2 Y + K = m\omega^2 A\cos\theta \tag{19}$$

$$-c_e\omega Y = -m\omega^2 A\sin\theta \tag{20}$$

where

$$K = k_1 Y + \frac{3}{4}k_3 Y^3 + \frac{10}{16}k_5 Y^5 + \frac{35}{64}k_7 Y^7 + \frac{126}{256}k_9 Y^9 \tag{21}$$

The amplitude-frequency response is derived by adding the squares of Eqs. (19) and (20):

$$(-m\omega^2 Y + K)^2 + (c_e\omega Y)^2 = (m\omega^2 A)^2 \tag{22}$$

Transmissibility is frequently employed to assess the suppression effectiveness. In the harmonic balance method, the absolute displacement y_1 of mass m is given by:

$$y_1 = y + y_0 = (Y + A\cos\theta)\cos\omega t - A\sin\theta\sin\omega t \tag{23}$$

Transmissibility:

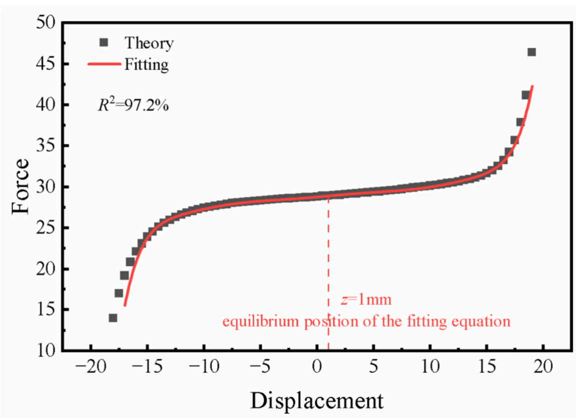

Fig. 11. Polynomial fitting of magnetic force.

$$T = \frac{|y_1|}{|y_0|} = \sqrt{1 + \frac{Y^2}{A^2} + 2\frac{Y}{A}\cos\theta} \tag{24}$$

where cosθ can be obtained from Eq. (19).

5.2. Transmissibility evaluation

Transmissibility is obtained by numerically solving Eq. (22)–(24). The force–displacement curve with $d = 0$ mm and $e = 20$ mm from Fig. 9(c) is used as an example. To improve the accuracy of the polynomial fitting, the equilibrium point is shifted to $z = 1$ mm. The load and stiffness coefficients are obtained through polynomial fitting, and the goodness of fit R^2, is used to evaluate the quality of the fitting, as shown in Fig. 11.

Fig. 12 shows how Coulomb friction and viscous damping influence vibration isolation performance under varying displacement excitations. In this section, Coulomb friction force f is set to 0, 0.5 and 1 N, viscous damping coefficient c is set to 3 and 9 Ns/m ($\xi =$ 0.11, 0.33), and the excitation amplitude A is set to 1, 5, and 9 mm. Fig. 12(a) indicates that, in the absence of friction, smaller viscous damping and larger excitation amplitudes result in strong nonlinear responses in the resonance region, leading to jump phenomena and higher transmissibility. This behavior is undesirable for engineering applications. At higher frequencies, transmissibility decreases linearly, where the transmissibility becomes independent of the excitation amplitude.

When considering a system with friction (Fig. 12(b) and (c)), three key observations emerge. First, at high excitation amplitudes, the isolator's response magnitude approaches that of the frictionless system, with aligning more closely at increasing amplitudes. Second, friction induces different response in the resonance region at lower amplitudes, compared to the frictionless system. Specifically, smaller excitation amplitudes lead to higher initial isolation frequencies, with larger friction resulting in a more pronounced increase. This behavior is attributed to the "self-locking" phenomenon of Coulomb friction systems [37,38]. In the small amplitude, low-frequency range, the driving force from the base is insufficient to overcome the frictional force, causing the isolation system to behave as a rigid connection and consequently lose its isolation capability. Third, isolator combining higher viscous damping with lower friction forces still exhibit relatively small resonance peaks, as shown in Fig. 12(b).

6. Experimental verification

This section develops an experimental prototype of the proposed isolator and sets up a testing system for evaluation. The static performance of the isolator was tested using a universal tensile testing machine, which tested both the magnetic constant-force and the force with repulsion boundaries. The dynamic performance was assessed by a vibration testing platform, with scanning frequency excitations at varying amplitudes.

6.1. Static experiment

The prototype of the proposed isolator is shown in Fig. 13, which includes a constant force magnet array, boundary magnetic rings, guide rails, and a base. The static measurements were conducted in a universal tensile testing machine, where the computer provided displacement signal and the built-in sensors of the machine recorded displacement and force.

Fig. 14 presents the measurement static testing results. Fig. 14(a) and (b) indicate the constant force range closely matches the design in Section 3.5, as well as the load variation trend. Fig. 14(c) illustrates the theoretical magnetic force curve and experimental measurements for the combination of a repulsion boundary gap of $e = 20$ and a stator sliding distance of $d = 0$. The overall trends of both curves are largely consistent. The proposed isolator also exhibits Coulomb friction in Fig. 14(c). Analysis indicates that the average friction force f is 0.54 N.

Although the trend is consistent, there are also numerical errors, primarily due to the following four factors. (I) Measurement errors in the magnetic parameter B_r. The value of B_r used in the theoretical model is inferred from the magnetic field measurement of the

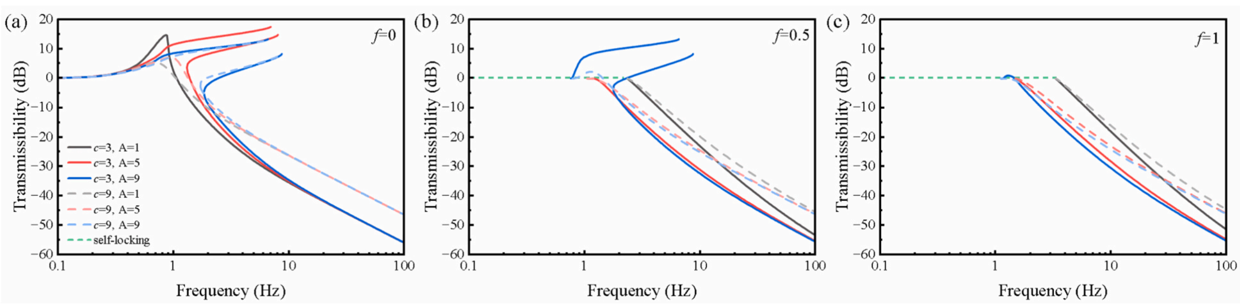

Fig. 12. Isolation performance under different working conditions: (a) Coulomb friction force $f = 0$ N, viscous damping coefficient c = 3, 9 Ns/m, excitation amplitude A = 1, 5, 9 mm, (b) $f = 0.5$ N and (c) $f = 1$ N.

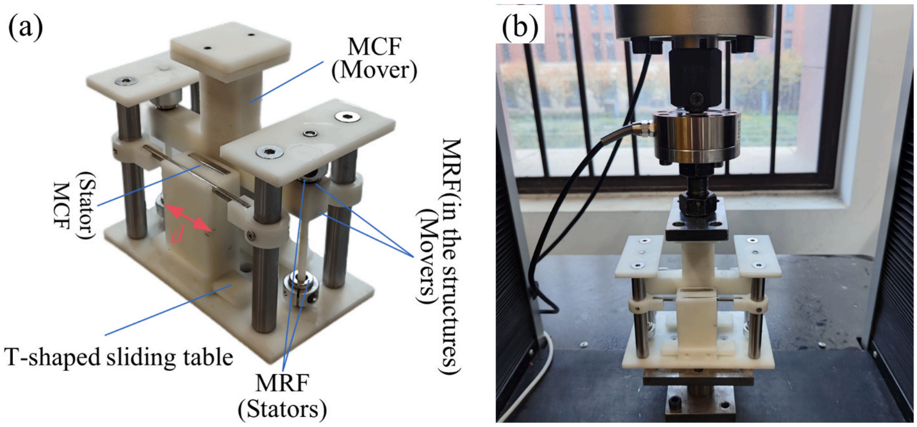

Fig. 13. (a) Prototype of vibration isolator and (b) static experimental testing.

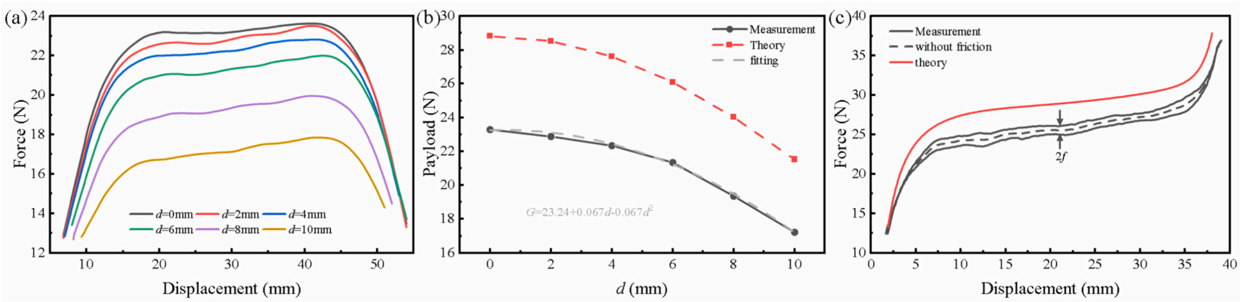

Fig. 14. Static test: (a) Force–displacement relation of constant force structure (without boundary), (b) comparison between experimental and theoretical loads and (c) with boundary.

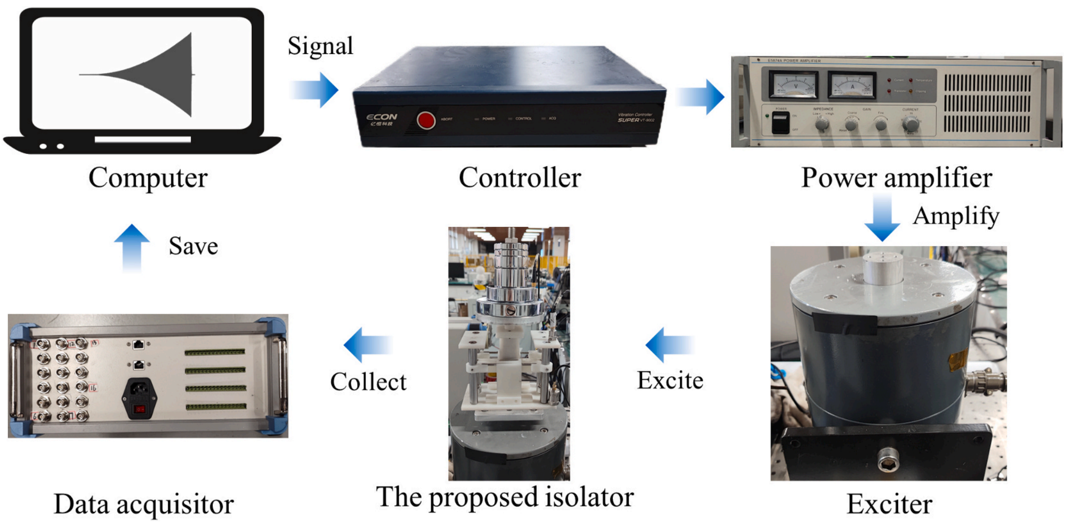

Fig. 15. Vibration testing experiment configuration.

magnet using a Gauss meter, which inevitably introduces measurement and instrument errors. (II) The assumption of a relative permeability $\mu_r = 1$ in the theoretical model. In practice, $\mu_r \neq 1$, leading to inherent deviations in the computation of magnetic fields and forces [48,58]. (III) The theoretical load does not account for the self-weight of the magnets and the mover structure. (IV) Limitations in machining accuracy and the material properties of the frame prevent the moving component from maintaining a perfectly constant air gap during motion.

6.2. Dynamic experiment

The vibration testing setup is shown in Fig. 15. The computer generated an excitation signal, which was sent to the controller (VT-9002–1). The signal was amplified by the power amplifier (YE5874A) before being provided as harmonic excitation to the isolator by the exciter (JZK-50). Two accelerometers (sensitivity of 100 mV/g) were installed on the load and base plate of the isolator. The acceleration signals were collected by a data collector.

The experiment was configured as a linearly increasing frequency scanning vibration test for the isolator, spanning a frequency range of 1.2–20 Hz, with a scanning rate of 5 Hz/min and a constant displacement excitation amplitude. Furthermore, to verify the isolation performance under different displacement excitation amplitudes, displacement excitation amplitudes were set to 1, 3, 5, 7 and 9 mm. In addition, to investigate isolation performance under varying loads, the experiment started with the maximum load (at stators' movement distance $d = 0$ mm) and gradually decreased in 200 g increments. And the sliding distance d of the variable load is determined using the fitted equation in Fig. 14(b).

Fig. 16(a)–(d) present a comparison of transmissibility for four different loads under varying displacement excitations. The results can be summarized into three key patterns:

(1) When the excitation is small, Coulomb friction seriously affects the isolation performance, causing a marked increase in the system's initial isolation frequency.
(2) As the excitation amplitude increases, the impact of Coulomb friction gradually weakens, and the system response approaches that of a system without hysteretic damping. At an excitation amplitude of 9 mm, the system's initial isolation frequency drops below 2 Hz, demonstrating the proposed isolator's exceptionally low natural frequency.
(3) Variations in load do not notably alter the isolation bandwidth and transmissibility.

Fig. 16 also presents a comparison between the theoretical and experimental transmissibility results. The parameters used in the theoretical model are taken from Table 3, supplemented by experimentally estimated damping parameters ($c = 3$ Ns/m, $f = 0.54$ N). The results indicate that under high excitation amplitudes, the discrepancies of transmissibility between the experimental and

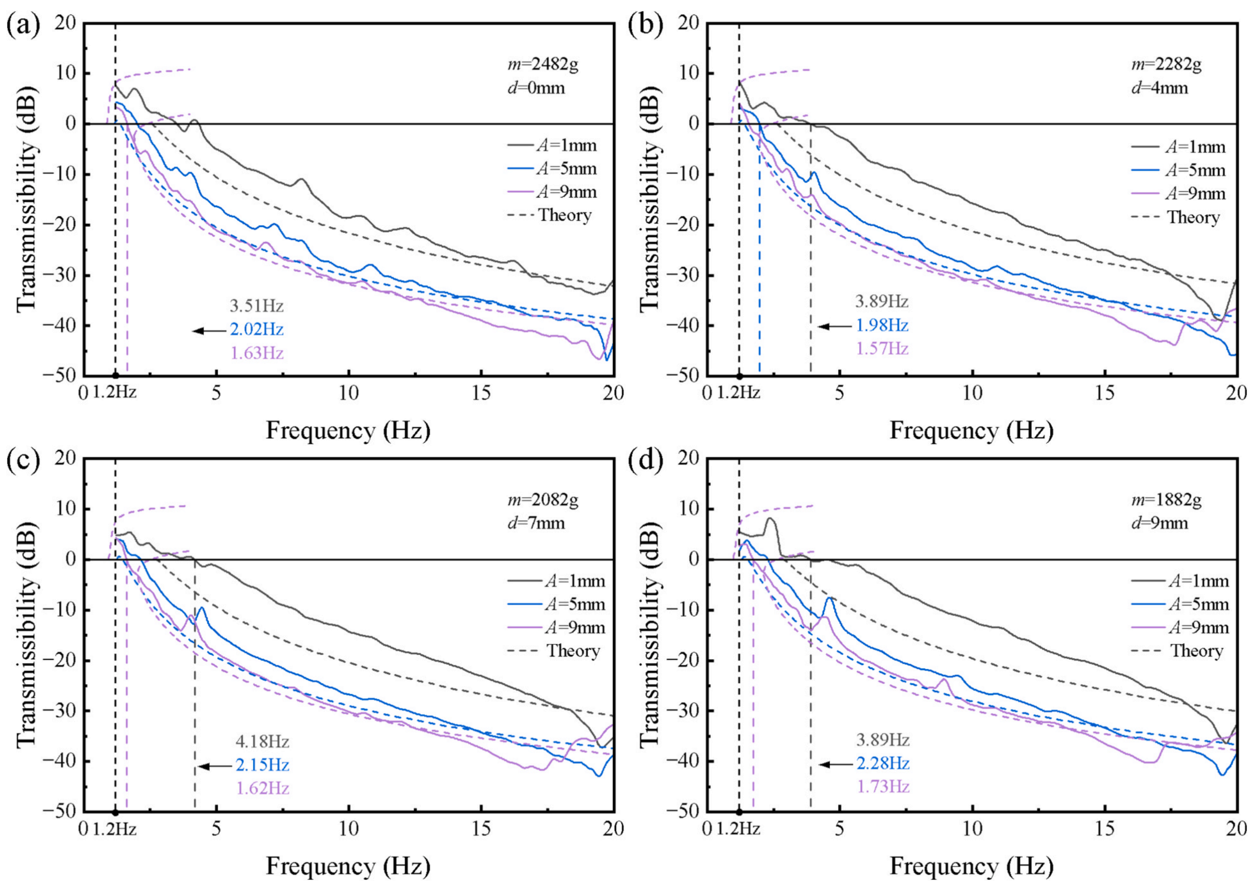

Fig. 16. Transmissibility of different loads with different excitation amplitudes: (a) $m = 2482$ g, $d = 0$ mm, (b) $m = 2282$ g, $d = 4$ mm, (c) $m = 2082$ g, $d = 7$ mm and (d) $m = 1882$ g, $d = 9$ mm.

Table 3
Fitting results of stiffness coefficient.

k_1 (N/m)	k_3 (N/m^3)	k_5 (N/m^5)	k_7 (N/m^7)	k_9 (N/m^9)
124	-1.223×10^6	2.355×10^{10}	-1.321×10^{14}	2.753×10^{17}

simulation are relatively small, demonstrating agreement. When the excitation amplitude is 9 mm, the theoretical initial isolation frequency (1.9 Hz) of the proposed isolator closely matches the experimental result (1.63 Hz). This suggests that the fitted stiffness coefficients in Table 3 effectively characterize the actual dynamic behavior of the system. However, under low excitation amplitudes, more pronounced deviations are observed. These differences are primarily attributed to assembly tolerances, particularly the clearance between the guide rail and the bearing. When both excitation frequency and amplitude are low, the driving force provided by the base and the inertial force of the mover are relatively small. In such conditions, imperfect contact between the guide rail and the bearing allows the mover to exhibit additional non-vertical vibrations. These non-ideal motions introduce lateral forces that increase Coulomb friction in the system, thereby disturbing the transmissibility characteristics at low amplitude and low frequency.

7. Conclusion

This article proposes a novel magnetic quasi-zero stiffness (QZS) isolator, which breaks through the limitations of traditional magnetic isolators due to the narrow QZS range caused by magnetic field nonlinearity and fixed load. Overall, the innovation and main conclusions of this design can be summarized as follows:

(1) The proposed isolator leverages the principles of uniform magnetic fields and constant current to achieve quasi-zero stiffness (QZS).
(2) The size and positional parameters of the magnets play a crucial role in determining the QZS region, load capacity, and the nonlinear behavior of force and stiffness. Therefore, careful selection of these parameters is essential for prototype fabrication.
(3) A dynamic model of the isolator was established, incorporating both viscous damping and Coulomb friction. The solution obtained using the harmonic balance method indicates that Coulomb friction significantly increases the initial isolation frequency at low excitation amplitudes. However, at higher excitation levels, the initial isolation frequency decreases, ultimately achieving an initial isolation frequency below 2 Hz.
(4) The performance of the prototype was validated through comprehensive static and dynamic experiments. The results demonstrated that the isolator exhibits excellent vibration isolation under large displacement excitations (up to 9 mm) and maintains a consistent isolation bandwidth and transmissibility under varying load conditions. Furthermore, the experiments confirmed the accuracy of the fitted relation between load and the relative distance of the stators.

CRediT authorship contribution statement

Jun Yuan: Writing – original draft, Methodology, Formal analysis, Data curation, Conceptualization. **Yunlai Zhou:** Writing – review & editing, Validation, Resources, Funding acquisition. **Ying Zhang:** Validation, Resources, Methodology, Funding acquisition, Conceptualization. **Magd Abdel Wahab:** Writing – review & editing, Supervision.

Declaration of competing interest

The authors declare that they have no known competing financial interests or personal relationships that could have appeared to influence the work reported in this paper.

Acknowledgements

This study was supported by the Youth Top Talent Program of Xi'an Jiaotong University, the Postdoctoral Fellowship Program of CPSF, China (Grant No. GZB20240602), the State Key Laboratory for Strength and Vibration of Mechanical Structures and the State Key Laboratory for Manufacturing System Engineering of Xi'an Jiaotong University.

Data availability

Data will be made available on request.

References

[1] C.E. Okwudire, J. Lee, Minimization of the residual vibrations of ultra-precision manufacturing machines via optimal placement of vibration isolators, Precis. Eng. 37 (2013) 425–432, https://doi.org/10.1016/j.precisioneng.2012.11.005.
[2] B. Voigtländer, P. Coenen, V. Cherepanov, P. Borgens, T. Duden, F.S. Tautz, Low vibration laboratory with a single-stage vibration isolation for microscopy applications, Rev. Sci. Instrum. 88 (2017), https://doi.org/10.1063/1.4975832.

[3] L. Li, L.Y. Tan, L. Kong, D. Wang, H.B. Yang, The influence of flywheel micro vibration on space camera and vibration suppression, Mech. Syst. Signal Process. 100 (2018) 360–370, https://doi.org/10.1016/j.ymssp.2017.07.029.
[4] G.B. Wang, Y. Yin, J.N. Wang, Vibration safety evaluation and vibration isolation control measures for buried oil pipelines under dynamic compaction: a case study, Soil Dyn. Earthq. Eng. 167 (2023), https://doi.org/10.1016/j.soildyn.2023.107783.
[5] T. Sheng, G.B. Liu, X.C. Bian, W.X. Shi, Y. Chen, Development of a three-directional vibration isolator for buildings subject to metro- and earthquake-induced vibrations, Eng. Struct. 252 (2022), https://doi.org/10.1016/j.engstruct.2021.113576.
[6] A. Carrella, M.J. Brennan, T.P. Waters, V. Lopes, Force and displacement transmissibility of a nonlinear isolator with high-static-low-dynamic-stiffness, Int. J. Mech. Sci. 55 (2012) 22–29, https://doi.org/10.1016/j.ijmecsci.2011.11.012.
[7] R.A. Ibrahim, Recent advances in nonlinear passive vibration isolators, J. Sound Vib. 314 (2008) 371–452, https://doi.org/10.1016/j.jsv.2008.01.014.
[8] A. Carrella, M.J. Brennan, T.P. Waters, Static analysis of a passive vibration isolator with quasi-zero-stiffness characteristic, J. Sound Vib. 301 (2007) 678–689, https://doi.org/10.1016/j.jsv.2006.10.011.
[9] A. Carrella, M.J. Brennan, I. Kovacic, T.P. Waters, On the force transmissibility of a vibration isolator with quasi-zero-stiffness, J. Sound Vib. 322 (2009) 707–717, https://doi.org/10.1016/j.jsv.2008.11.034.
[10] I. Kovacic, M.J. Brennan, T.P. Waters, A study of a nonlinear vibration isolator with a quasi-zero stiffness characteristic, J. Sound Vib. 315 (2008) 700–711, https://doi.org/10.1016/j.jsv.2007.12.019.
[11] T.D. Le, K.K. Ahn, Experimental investigation of a vibration isolation system using negative stiffness structure, Int. J. Mech. Sci. 70 (2013) 99–112, https://doi.org/10.1016/j.ijmecsci.2013.02.009.
[12] H. Ding, J.C. Ji, L.Q. Chen, Nonlinear vibration isolation for fluid-conveying pipes using quasi-zero stiffness characteristics, Mech. Syst. Signal Process. 121 (2019) 675–688, https://doi.org/10.1016/j.ymssp.2018.11.057.
[13] X.T. Liu, X.C. Huang, H.X. Hua, On the characteristics of a quasi-zero stiffness isolator using Euler buckled beam as negative stiffness corrector, J. Sound Vib. 332 (2013) 3359–3376, https://doi.org/10.1016/j.jsv.2012.10.037.
[14] B.A. Fulcher, D.W. Shahan, M.R. Haberman, C.C. Seepersad, P.S. Wilson, Analytical and Experimental Investigation of Buckled Beams as negative Stiffness elements for Passive Vibration and shock Isolation Systems, J. Vib. Acoust. 136 (2014), https://doi.org/10.1115/1.4026888.
[15] S. Dalela, P.S. Balaji, D.P. Jena, Design of a metastructure for vibration isolation with quasi-zero-stiffness characteristics using bistable curved beam, Nonlinear Dyn. 108 (2022) 1931–1971, https://doi.org/10.1007/s11071-022-07301-0.
[16] W.J. Wu, X.D. Chen, Y.H. Shan, Analysis and experiment of a vibration isolator using a novel magnetic spring with negative stiffness, J. Sound Vib. 333 (2014) 2958–2970, https://doi.org/10.1016/j.jsv.2014.02.009.
[17] Y.S. Zheng, X.N. Zhang, Y.J. Luo, B. Yan, C.C. Ma, Design and experiment of a high-static-low-dynamic stiffness isolator using a negative stiffness magnetic spring, J. Sound Vib. 360 (2016) 31–52, https://doi.org/10.1016/j.jsv.2015.09.019.
[18] B. Yan, H.Y. Ma, C.X. Zhao, C.Y. Wu, K. Wang, P.F. Wang, A vari-stiffness nonlinear isolator with magnetic effects: Theoretical modeling and experimental verification, Int. J. Mech. Sci. 148 (2018) 745–755, https://doi.org/10.1016/j.ijmecsci.2018.09.031.
[19] G.X. Dong, X.N. Zhang, S.L. Xie, B. Yan, Y.J. Luo, Simulated and experimental studies on a high-static-low-dynamic stiffness isolator using magnetic negative stiffness spring, Mech. Syst. Signal Process. 86 (2017) 188–203, https://doi.org/10.1016/j.ymssp.2016.09.040.
[20] J.X. Zhou, X.L. Wang, D.L. Xu, S. Bishop, Nonlinear dynamic characteristics of a quasi-zero stiffness vibration isolator with cam-roller-spring mechanisms, J. Sound Vib. 346 (2015) 53–69, https://doi.org/10.1016/j.jsv.2015.02.005.
[21] Y.H. Yao, H.G. Li, Y. Li, X.J. Wang, Analytical and experimental investigation of a high-static-low-dynamic stiffness isolator with cam-roller-spring mechanism, Int. J. Mech. Sci. 186 (2020), https://doi.org/10.1016/j.ijmecsci.2020.105888.
[22] S. Zuo, D.Y. Wang, Y.S. Zhang, Q.T. Luo, Design and testing of a parabolic cam-roller quasi-zero-stiffness vibration isolator, Int. J. Mech. Sci. 220 (2022), https://doi.org/10.1016/j.ijmecsci.2022.107146.
[23] J.L. Wu, L.Z. Zeng, B. Han, Y.F. Zhou, X. Luo, X.Q. Li, X.D. Chen, W. Jiang, Analysis and design of a novel arrayed magnetic spring with high negative stiffness for low-frequency vibration isolation, Int. J. Mech. Sci. 216 (2022), https://doi.org/10.1016/j.ijmecsci.2021.106980.
[24] Y. Zhang, Q.H. Liu, Y.G. Lei, J.Y. Cao, W.H. Liao, Halbach high negative stiffness isolator: Modeling and experiments, Mech. Syst. Signal Process. 188 (2023), https://doi.org/10.1016/j.ymssp.2022.110014.
[25] Y. Zhang, Q.H. Liu, Y.G. Lei, J.Y. Cao, W.H. Liao, Circular Halbach negative stiffness isolating from torsional vibration: Design, modeling and experiments, Mech. Syst. Signal Process. 202 (2023), https://doi.org/10.1016/j.ymssp.2023.110711.
[26] M.K. Wu, R.Q. Gao, Y.F. Zhou, J.X. Che, J.L. Wu, X.Q. Li, X.D. Chen, W. Jiang, Analysis and experiment of a multi-tile magnetic spring with high negative stiffness, Mech. Syst. Signal Process. 223 (2025), https://doi.org/10.1016/j.ymssp.2024.111914.
[27] F. Zhao, J.C. Ji, K. Ye, Q.T. Luo, Increase of quasi-zero stiffness region using two pairs of oblique springs, Mech. Syst. Signal Process. 144 (2020), https://doi.org/10.1016/j.ymssp.2020.106975.
[28] F. Zhao, J.C. Ji, K. Ye, Q.T. Luo, An innovative quasi-zero stiffness isolator with three pairs of oblique springs, Int. J. Mech. Sci. 192 (2021), https://doi.org/10.1016/j.ijmecsci.2020.106093.
[29] F. Zhao, J.C. Ji, Q.T. Luo, S.Q. Cao, L.M. Chen, W.L. Du, An improved quasi-zero stiffness isolator with two pairs of oblique springs to increase isolation frequency band, Nonlinear Dyn. 104 (2021) 349–365, https://doi.org/10.1007/s11071-021-06296-4.
[30] K. Ye, J.C. Ji, T. Brown, Design of a quasi-zero stiffness isolation system for supporting different loads, J. Sound Vib. 471 (2020), https://doi.org/10.1016/j.jsv.2020.115198.
[31] G. Yan, H.X. Zou, S. Wang, L.C. Zhao, Q.H. Gao, T. Tan, W.M. Zhan, Large stroke quasi-zero stiffness vibration isolator using three-link mechanism, J. Sound Vib. 478 (2020), https://doi.org/10.1016/j.jsv.2020.115344.
[32] Y.J. Xie, F. Niu, J.G. Sun, L.S. Meng, Design and Analysis of a Novel Quasi-Zero Stiffness Isolator under Variable Loads, Math. Probl. Eng. 2022 (2022), https://doi.org/10.1155/2022/9082752.
[33] Y. Wang, X.J. Jing, H.H. Dai, F.M. Li, Subharmonics and ultra-subharmonics of a bio-inspired nonlinear isolation system, Int. J. Mech. Sci. 152 (2019) 167–184, https://doi.org/10.1016/j.ijmecsci.2018.12.054.
[34] Y. Wang, X.J. Jing, Y.Q. Guo, Nonlinear analysis of a bio-inspired vertically asymmetric isolation system under different structural constraints, Nonlinear Dyn. 95 (2019) 445–464, https://doi.org/10.1007/s11071-018-4575-5.
[35] Z.J. Wu, X.J. Jing, J. Bian, F.M. Li, R. Allen, Vibration isolation by exploring bio-inspired structural nonlinearity, Bioinspir. Biomim. 10 (2015), https://doi.org/10.1088/1748-3190/10/5/056015.
[36] T.C. Deng, G.L. Wen, H. Ding, Z.Q. Lu, L.Q. Chen, A bio-inspired isolator based on characteristics of quasi-zero stiffness and bird multi-layer neck, Mech. Syst. Signal Process. 145 (2020), https://doi.org/10.1016/j.ymssp.2020.106967.
[37] A.D. Shaw, G. Gatti, P.J.P. Gonçalves, B. Tang, M.J. Brennan, Frictional phenomena within a quasi zero stiffness vibration device, Mech. Syst. Signal Process. 211 (2024), https://doi.org/10.1016/j.ymssp.2024.111113.
[38] X.T. Liu, Q. Zhao, Z.Y. Zhang, X.B. Zhou, An experiment investigation on the effect of Coulomb friction on the displacement transmissibility of a quasi-zero stiffness isolator, J. Mech. Sci. Technol. 33 (2019) 121–127, https://doi.org/10.1007/s12206-018-1212-7.
[39] X. Liu, S. Chen, B. Wang, X.J. Tan, L. Yu, A compact quasi-zero-stiffness mechanical metamaterial based on truncated conical shells, Int. J. Mech. Sci. 277 (2024), https://doi.org/10.1016/j.ijmecsci.2024.109390.
[40] Q.D. Lin, J.X. Zhou, K. Wang, D.L. Xu, G.L. Wen, Q. Wang, Three-dimensional quasi-zero-stiffness metamaterial for low-frequency and wide complete band gap, Compos. Struct. 307 (2023), https://doi.org/10.1016/j.compstruct.2022.116656.
[41] J.H. Zhou, J.X. Zhou, H.B. Pan, K. Wang, C.Q. Cai, G.L. Wen, Multi-layer quasi-zero-stiffness meta-structure for high-efficiency vibration isolation at low frequency, Appl. Math. Mech.-Engl. 45 (2024) 1189–1208, https://doi.org/10.1007/s10483-024-3157-6.
[42] C.Q. Cai, J.X. Zhou, L.C. Wu, K. Wang, D.L. Xu, H.J. Ouyang, Design and numerical validation of quasi-zero-stiffness metamaterials for very low-frequency band gaps, Compos. Struct. 236 (2020), https://doi.org/10.1016/j.compstruct.2020.111862.

[43] Q. Zhang, D.K. Guo, G.K. Hu, Tailored Mechanical Metamaterials with Programmable Quasi-Zero-Stiffness Features for Full-Band Vibration Isolation, Adv. Funct. Mater. 31 (2021), https://doi.org/10.1002/adfm.202101428.
[44] C.J. Zeng, L.W. Liu, Y.Q. Hu, W. Zhao, X.Z. Xin, Y.J. Liu, J.S. Leng, Stair-Stepping Mechanical Metamaterials with Programmable load Plateaus, Adv. Funct. Mater. (2024), https://doi.org/10.1002/adfm.202408887.
[45] S. Hou, J.Z. Wei, A quasi-zero stiffness mechanism with monolithic flexible beams for low-frequency vibration isolation, Mech. Syst. Signal Process. 210 (2024), https://doi.org/10.1016/j.ymssp.2024.111154.
[46] L.L. Wu, Y. Wang, Z.R. Zhai, Y. Yang, D. Krishnaraju, J.Q. Lu, F.G. Wu, Q.X. Wang, H.Q. Jiang, Mechanical metamaterials for full-band mechanical wave shielding, Appl. Mater. Today 20 (2020), https://doi.org/10.1016/j.apmt.2020.100671.
[47] Z.Y. Sun, X.H. Yue, A. Li, X. Yin, Z.Y. Gao, L.Y. Zhang, A tensegrity-based torsional vibration isolator with broad quasi-zero-stiffness region, Mech. Syst. Signal Process. 224 (2025), https://doi.org/10.1016/j.ymssp.2024.112215.
[48] H. Zhang, Y.X. Lou, L.S. Zhou, Z.Q. Kou, J.R. Mu, Modeling and Optimization of a Large-load magnetic Levitation Gravity Compensator, IEEE Trans. Ind. Electron. 70 (2023) 5055–5064, https://doi.org/10.1109/Tie.2022.3183365.
[49] R.Q. Gao, J.X. Che, M.K. Wu, W. Zhang, X.Y. Xie, J.L. Wu, X.D. Chen, W. Jiang, Axial-offset magnetic negative stiffness spring with high density and linearity, Int. J. Mech. Sci. 287 (2025), https://doi.org/10.1016/j.ijmecsci.2025.109989.
[50] B. Yan, N. Yu, Z.H. Wang, C.A.Y. Wu, S. Wang, W.M. Zhang, Lever-type quasi-zero stiffness vibration isolator with magnetic spring, J. Sound Vib. 527 (2022), https://doi.org/10.1016/j.jsv.2022.116865.
[51] J.J. Lu, G. Yan, W.H. Qi, H. Yan, J.W. Shi, A. Chen, W.M. Zhang, Load-adaptive quasi-zero stiffness vibration isolation via dual electromagnetic stiffness regulation, J. Sound Vib. 567 (2023), https://doi.org/10.1016/j.jsv.2023.118059.
[52] W.H. Qi, G. Yan, J.J. Lu, H. Yan, J.W. Shi, X.S. Wei, S. Wang, W.M. Zhang, Magnetically modulated sliding structure for low frequency vibration isolation, J. Sound Vib. 526 (2022), https://doi.org/10.1016/j.jsv.2022.116819.
[53] L.W. Ji, Y.J. Luo, Y.H. Zhang, S.L. Xie, M.L. Xu, A creative wide-frequency and large-amplitude vibration isolator design method based on magnetic negative stiffness and displacement amplification mechanism, J. Sound Vib. 572 (2024), https://doi.org/10.1016/j.jsv.2023.118185.
[54] W.H. Qi, F.R. Liu, J.J. Lu, T.Y. Zhao, H. Yan, G. Yan, W.M. Zhang, Generative quasi-zero stiffness paradigm for vibration isolation by constraining the constant force with hardening boundaries, J. Sound Vib. 589 (2024), https://doi.org/10.1016/j.jsv.2024.118548.
[55] C.R. Liu, Y.W. Wang, W. Zhang, K.P. Yu, J.J. Mao, H. Shen, Nonlinear dynamics of a magnetic vibration isolator with higher-order stable quasi-zero-stiffness, Mech. Syst. Signal Process. 218 (2024), https://doi.org/10.1016/j.ymssp.2024.111584.
[56] G. Akoun, J.P. Yonnet, 3D ANALYTICAL CALCULATION OF THE FORCES EXERTED BETWEEN 2 CUBOIDAL MAGNETS, IEEE Trans. Magn. 20 (1984) 1962–1964, https://doi.org/10.1109/tmag.1984.1063554.
[57] Y. Zhang, W. Wang, J. Cao, Semi-analytical Expression of Force and Stiffness of Perpendicular Polarized Ring Magnets for Nonlinear Dynamic Analysis, Advances in Applied Nonlinear Dynamics, Vibration, and Control - 2023: The Proceedings of 2023 International Conference on Applied Nonlinear Dynamics, Vibration, and Control (ICANDVC2023). Lecture Notes in Electrical Engineering (1152), (2024) 25-38. doi:10.1007/978-981-97-0554-2_3.
[58] J.Z. Li, Q. Liu, L. Wang, S.T. Wang, J. Wang, Considering Operating Point Variation in 3-D Analytical Charge Model used for Design of Low-Stiffness Permanent Magnet Vibration Isolator, IEEE Trans. Ind. Electron. 67 (2020) 6732–6741, https://doi.org/10.1109/Tie.2019.2934056.